Publication Year	2022
Acceptance in OA	2025-02-21T18:57:29Z
Title	The Coma Cluster at LOFAR Frequencies. II. The Halo, Relic, and a New Accretion Relic
Authors	BONAFEDE, Annalisa, BRUNETTI, Gianfranco, Rudnick, L., VAZZA, Franco, Bourdin, H., GIOVANNINI, Gabriele, Shimwell, T. W., Zhang, X., Mazzotta, P., Simionescu, A., Biava, N., Bonnassieux, E., BRIENZA, Marisa, Brüggen, M., Rajpurohit, K., Riseley, C. J., Stuardi, C., Feretti, L., Tasse, C., BOTTEON, Andrea, CARRETTI, Ettore, CASSANO, Rossella, Cuciti, V., DE GASPERIN, Francesco, GASTALDELLO, Fabio, ROSSETTI, Mariachiara, Rottgering, H. J. A., VENTURI, Tiziana, van Weeren, R. J.
Publisher's version (DOI)	10.3847/1538-4357/ac721d
Handle	http://hdl.handle.net/20.500.12386/36138
Journal	THE ASTROPHYSICAL JOURNAL
Volume	933

The Astrophysical Journal, 933:218 (25pp), 2022 July 10 https://doi.org/10.3847/1538-4357/ac721d

The Coma Cluster at LOFAR Frequencies. II. The Halo, Relic, and a New Accretion Relic

A. Bonafede[1,2,3], G. Brunetti[2], L. Rudnick[4], F. Vazza[1,2,3], H. Bourdin[5,6], G. Giovannini[1,2], T. W. Shimwell[7,8], X. Zhang[8,9], P. Mazzotta[5,6], A. Simionescu[8,9,10], N. Biava[1,2], E. Bonnassieux[1,2], M. Brienza[1,2], M. Brüggen[3], K. Rajpurohit[1,2,11], C. J. Riseley[1,2,12], C. Stuardi[1,2], L. Feretti[2], C. Tasse[13,14], A. Botteon[8], E. Carretti[2], R. Cassano[2], V. Cuciti[3], F. de Gasperin[2,3], F. Gastaldello[15], M. Rossetti[15], H. J. A. Rottgering[8], T. Venturi[2], and R. J. van Weeren[8]
[1] DIFA—Università di Bologna, via Gobetti 93/2, I-40129 Bologna, Italy; annalisa.bonafede@unibo.it
[2] INAF—IRA, Via Gobetti 101, I-40129 Bologna, Italy; IRA—INAF, via P. Gobetti 101, I-40129 Bologna, Italy
[3] Universität Hamburg, Hamburger Sternwarte, Gojenbergsweg 112, D-21029, Hamburg, Germany
[4] Minnesota Institute for Astrophysics, School of Physics and Astronomy, University of Minnesota, Minneapolis, MN 55455, USA
[5] Università di Roma Tor Vergata, Via della Ricerca Scientifica, I-00133 Roma, Italy
[6] INFN, Sezione di Roma 2, Università di Roma Tor Vergata, Via della Ricerca Scientifica, 1, Roma, Italy
[7] ASTRON, Netherlands Institute for Radio Astronomy, Oude Hoogeveensedijk 4, 7991 PD, Dwingeloo, The Netherlands
[8] Leiden Observatory, Leiden University, PO Box 9513, 2300 RA Leiden, The Netherlands
[9] SRON Netherlands Institute for Space Research, Niels Bohrweg 4, 2333 CA Leiden, The Netherlands
[10] Kavli Institute for the Physics and Mathematics of the Universe (WPI), The University of Tokyo, Kashiwa, Chiba 277-8583, Japan
[11] Thüringer Landessternwarte, Sternwarte 5, D-07778 Tautenburg, Germany
[12] CSIRO Space & Astronomy, PO Box 1130, Bentley, WA 6102, Australia
[13] GEPI and USN, Observatoire de Paris, Université PSL, CNRS, 5 Place Jules Janssen, F-92190 Meudon, France
[14] Department of Physics and Electronics, Rhodes University, PO Box 94, Grahamstown, 6140, South Africa
[15] INAF—IASF Milano, via A. Corti 12, I-20133 Milano, Italy

Received 2022 March 2; revised 2022 May 16; accepted 2022 May 17; published 2022 July 15

Abstract

We present LOw Frequency ARray observations of the Coma Cluster field at 144 MHz. The cluster hosts one of the most famous radio halos, a relic, and a low surface brightness bridge. We detect new features that allow us to make a step forward in the understanding of particle acceleration in clusters. The radio halo extends for more than 2 Mpc, which is the largest extent ever reported. To the northeast of the cluster, beyond the Coma virial radius, we discover an arc-like radio source that could trace particles accelerated by an accretion shock. To the west of the halo, coincident with a shock detected in the X-rays, we confirm the presence of a radio front, with different spectral properties with respect to the rest of the halo. We detect a radial steepening of the radio halo spectral index between 144 and 342 MHz, at ~30′ from the cluster center, that may indicate a non-constant re-acceleration time throughout the volume. We also detect a mild steepening of the spectral index toward the cluster center. For the first time, a radial change in the slope of the radio–X-ray correlation is found, and we show that such a change could indicate an increasing fraction of cosmic-ray versus thermal energy density in the cluster outskirts. Finally, we investigate the origin of the emission between the relic and the source NGC 4789, and we argue that NGC 4789 could have crossed the shock originating the radio emission visible between its tail and the relic.

Unified Astronomy Thesaurus concepts: Galaxy clusters (584); Non-thermal radiation sources (1119); Extragalactic radio sources (508); Intracluster medium (858)

1. Introduction

Diffuse, non-thermal emission has been observed in more than 100 clusters of galaxies, revealing the existence of magnetic fields and relativistic particles on scales as large as a few megaparsecs. In the past decade, the advent of low-frequency, sensitive radio observations has brought about a major advance in the discovery of these objects and the characterization of their properties.

Synchrotron emission from the intracluster medium (ICM) has been observed in the form of giant radio halos, mini halos, and radio relics, depending on their location and morphology. Giant radio halos are found at the centers of merging galaxy clusters, co-spatial with the X-ray emitting gas, and with sizes of 1–2 Mpc. Mini halos only have sizes of a few hundred kiloparsecs and are found mostly in cool-core clusters. Finally, radio relics are arc-like sources located in cluster outskirts, where they trace merger shock waves. We refer to van Weeren et al. (2019) for a recent review.

Since their discovery, it has been proposed that radio halos and relics are generated by shocks and turbulence driven in the ICM by cluster mergers (see, e.g., Brunetti & Jones 2014 for a review, and references therein). Although the details of the proposed mechanisms are not understood yet, radio halos have preferentially been found in merging clusters, supporting a connection between mergers and radio emission (Cuciti et al. 2015), and radio relics are often coincident with gas discontinuities detected in the X-ray and Sunyaev–Zel'dovich (SZ) images (e.g., Ogrean et al. 2013; Planck Collaboration et al. 2013). The origin of mini halos is still debated. They could originate either from turbulent motions that develop in the cluster core (e.g., ZuHone et al. 2013) or from hadronic collisions between cosmic-ray protons and thermal protons (e.g., Pfrommer & Enßlin 2004).

In the past years, the picture has become more complicated, and it has been found that some clusters with mini halos also host a larger-scale radio component, resembling a dimmer version of the giant radio halos but in non-merging objects (e.g., Savini et al. 2019; Raja et al. 2020). Moreover, a giant halo has also been found in a strong cool-core cluster, CL 1821+643 (Bonafede et al. 2014). In addition, relics and halos are sometimes connected through low-brightness radio bridges (van Weeren et al. 2012; Bonafede et al. 2021) that could be powered by mechanisms similar to those that are currently used to explain radio halos. On even larger scales, giant bridges of radio emission have been discovered, connecting massive clusters in a pre-merging state (e.g., Govoni et al. 2019; Botteon et al. 2020b).

Despite the differences between these types of sources, they all have a low surface brightness ($\sim 1 \mu$Jy arcsec^{-2}) at GHz frequencies. They also have steep radio spectra,[16] with a spectral index $\alpha < -1$ that makes them brighter at low radio frequencies. Hence, the advent of deep, low-frequency radio surveys, such as the LOFAR Two-meter Sky Survey (LoTSS; Shimwell et al. 2017, 2019), has both increased the number of new detections (see, e.g., Biava et al. 2021; Riseley et al. 2022; Botteon et al. 2022; Hoang et al. 2022) and allowed the study of known objects with unprecedented sensitivity and detail.

The Coma cluster hosts the most famous and best studied radio halo, as well as a radio relic and a radio bridge connecting the two (see Figure 1). The emission from the Coma field has been the subject of many studies since its discovery (e.g., Large et al. 1959; Ballarati et al. 1981; Giovannini et al. 1991; Venturi et al. 1990; Kronberg et al. 2007; Brown & Rudnick 2011). In Paper I (Bonafede et al. 2021), we have analyzed the properties of the radio bridge and have shown under which conditions it can be powered by turbulent acceleration. In this paper, we focus on the radio halo and relic of the Coma cluster. New LOFAR data give us information in regions that have been so far inaccessible, providing important clues on the origin of the radio emission. Giovannini et al. (1993) first found that the spectrum of the halo between 326 MHz and 1.28 GHz is characterized by two different regions: a central one with $\alpha \sim -0.8$, and a peripheral one with $\alpha \sim -1.2$. The integrated spectrum, computed between 30 MHz and 4.8 GHz, shows a high-frequency steepening consistent with homogeneous in situ re-acceleration models. They also reported a smooth distribution of the radio surface brightness, with no evidence for substructures at the resolution of ~50″. Their results have been confirmed later on by several authors, such as Thierbach et al. (2003), who complemented the analysis with observations up to 4.8 GHz, where the halo is barely detected. The steepening of the halo at high frequencies has been subject to debate, as the decrement due to the SZ effect was initially not accounted for. After the observation of the SZ effect by the Planck satellite (Planck Collaboration et al. 2011, 2014), it has been possible to confirm the steepening of the radio emission (Brunetti et al. 2013). However, we note that data below 300 MHz, being taken in the 1980s, lack the sensitivity, resolution, calibration, and imaging accuracy that are allowed by present instruments and techniques. In particular, the observation at 151 MHz (Cordey 1985), i.e., the closest in frequency to LOFAR High Band Array (HBA), has a resolution of ~70″ and a sensitivity of a few ×10 mJy beam^{-1}, which allowed the detection of the central part of the halo only. Similarly, observations at 43 and 73 MHz by Hanisch & Erickson (1980) did not allow us to properly subtract the emission from radio galaxies present in the cluster.

In addition to integrated spectral studies, better resolved spatial analysis of radio halos' spectral properties yields important information about the distribution of the component in the ICM (e.g., Rajpurohit et al. 2020, 2021a, 2021b). The halo in the Coma cluster offers a unique chance to perform spatially resolved studies of the halo brightness and of its connection between thermal and non-thermal plasma (e.g., Govoni et al. 2001; Brown & Rudnick 2011). So far, these studies have been inhibited by the lack of resolution, as it is often necessary to convolve the radio images with large Gaussian beams to recover the full halo emission.

LOFAR (van Haarlem et al. 2013), thanks to its sensitivity and resolution, provides a step forward for precise measurements of the halo size and flux density and for resolved studies. In this paper, we study the radio emission from the Coma cluster at 144 MHz, using data from LoTSS (Shimwell et al. 2019; Shimwell et al., in press) after ad hoc reprocessing. We also use published data and reprocessed archival X-ray and radio observations to perform a multiwavelength study of the emission.

This paper is organized as follows: In Section 2 we describe the observations and data reduction procedures. In Section 3 we present the main sources of diffuse emission, both known and newly discovered. The radio halo is analyzed in Section 4, its spectrum is analyzed in Section 5, and its correlation with the thermal gas is shown in Sections 6 and 7. In particular, in Sections 5.3 and 6.4, the halo properties, as discussed in the framework of turbulent re-acceleration models, and constraints to the model parameters are derived. In Section 8, we use cosmological MHD simulations to reproduce the thermal/non-thermal properties of the Coma cluster. In Section 9, the halo front is analyzed and its origin is discussed in connection with the shock wave found by X-ray and SZ studies. We also analyze the emission detected between the relic and the radio galaxy NGC 4789 in Section 10. Finally, results are discussed in Section 11. Throughout this paper, we use a ΛCDM cosmological model, with $\Omega_\Lambda = 0.714$, $H_0 = 69.6$ km s^{-1} Mpc^{-1}. At the Coma redshift ($z = 0.0231$) the angular to linear scale is 0.469 kpc arcsec^{-1} and the luminosity distance $D_L = 101.3$ Mpc.

2. Observations Used in This Work

2.1. LOFAR Data and Data Reduction

The data used in this work are part of the LoTSS (Shimwell et al. 2019, Shimwell et al. 2022) and consist of two pointings of 8 hr each taken with LOFAR (van Haarlem et al. 2013) HBA antennas, in the DUAL_INNER mode configuration. Each pointing is 8 hr long, bookended by 10-minute observations of a calibrator (3C 196), used to correct for the ionospheric Faraday rotation, clock offsets, instrumental XX and YY phase offsets, and time-independent amplitude solutions. The pointings are specified in Table 1, together with the distance from the central source NGC 4874, at the cluster center. Observations are centered at 144 MHz and have a 48 MHz total bandwidth. After preprocessing and direction-independent calibration, data are averaged into 24 visibility files, each

---

[16] Throughout this paper, we define the spectral index α as $S(\nu) \propto \nu^{\alpha}$, where S is the flux density at the frequency ν.

Figure 1. Composite IR-radio image of the Coma cluster field. In white the IR image in bands 1, 2, and 3 of the Wide-field Infrared Survey Explorer is shown. The red-orange color scale shows the composite radio image of the diffuse emission at 1′ for the diffuse emission and of 20″ for the sources in the field.

Table 1
LOFAR Observations Details

LoTSS Pointing	R.A. (deg)	Decl. (deg)	Time (hr)	Dist. of NGC 4874 (deg)
P192+27	192.945	27.2272	8	1.88
P195+27	195.856	27.2426	8	1.11

having a bandwidth of 1.953 MHz with a frequency resolution of 97.6 kHz and a time resolution of 8 s. For details about preprocessing and direction-independent calibration steps, we refer to Shimwell et al. (2019), where LoTSS data acquisition and processing are both explained in detail. The direction-dependent calibration has been made using the LoTSS DR2 pipeline, but with a slightly different procedure to account for the large-scale emission present in the Coma field. Specifically, we have included all baselines in imaging and calibration, while the LoTSS DR2 pipeline applies an inner *uv*-cut of the visibilities below 100 m to eliminate radio frequency interferences on the shortest baselines and filter out large-scale Galactic emission that would make the process of calibration and imaging more difficult. The two pointings have been calibrated separately, and unrelated sources have been subtracted from the visibilities through a multistep procedure, for which we refer the reader to Bonafede et al. (2021). Briefly, we first subtracted all the sources outside a radius of 1.5° centered on the cluster, using the model components obtained from an image at 20″ resolution with no inner *uv*-cut, and using a threshold of 5σ (0.75 mJy beam^{-1}). The subtracted data have been reimaged using a *uv*-cut of 300 m to filter out the diffuse emission from the ICM, and the model components have been subtracted using a threshold of 0.6 mJy beam^{-1}. Data have been reimaged again to check for the presence of residual emission from discrete sources using a *uv*-cut of 100 m. Residual emission associated with Active Galactic Nuclei (AGN) and sources unrelated to the halo and relic emission has been identified and subtracted by the data. The sources NGC 4789 and NGC 4839 have not been subtracted in order to study how their emission is connected to the relic and bridge, respectively. Two diffuse patches of emission to the west of Coma are still present and have been deconvolved in the imaging runs. They are discussed in the following sections.

The images used in this work have been done in a different way than in Bonafede et al. (2021), taking advantage of the new implementations that have been added to the imaging software in the past months. Imaging has been done with DDFacet (Tasse et al. 2018), using the recently added features that allow us to deconvolve large-scale emission in joint-deconvolution mode. We used the Sub Space Deconvolution (SSD) algorithm (Tasse et al. 2018 and references therein) to better model the clean components. Typically, four major cycles were needed to achieve a noise-like residual map. The

Table 2
Images Used in This Work

Image Name	Freq. (MHz)	Resolution	$\sigma_{\rm rms}$ (mJy beam^{-1})	Figure
LOFAR as LoTSS 6	144	$6'' \times 6''$	0.1	Figure 5
LOFAR as LoTSS 20	144	$20'' \times 20''$	0.15	Figure 3
LOFAR 35″	144	$35'' \times 35''$	0.2	Figure 3 (top panel), Figure 5
LOFAR 1′	144	$60'' \times 60''$	0.4	Figure 2
WSRT H	342	$134'' \times 68''$	0.4	Brown & Rudnick (2011)
LOFAR as WSRT H	144	$134'' \times 68''$	1.5	Figure 20
WSRT R	326	$150'' \times 100''$	1.2	Giovannini et al. (1991), Bonafede et al. (2021)
LOFAR as WSRT R	144	$150'' \times 100''$	1	

beam correction has been applied in the image plane, interpolating the beams of the two different pointings in the direction of Coma. Different images have been produced, as listed in Table 2, at various resolutions to highlight the emission from discrete sources and from the diffuse emission. To align the flux scale to LoTSS, we have extracted the fluxes from the sources in the Coma field and followed the same bootstrap procedure described in Hardcastle et al. (2016), which is based on the NRAO VLA Sky Survey (NVSS; Condon et al. 1998).

2.2. XMM-Newton and ROSAT Data

We used the XMM-Newton Science Analysis System (SAS) v18.0.0 for data reduction. The ObsIDs we used are listed in the Appendix. Event files from the MOS and pn detectors were generated from the observation data files with the tasks `emproc` and `epproc`. The out-of-time (OoT) events of pn were corrected following the user guide.[17] We used stacked Filter Wheel Closed (FWC) event files to generate non-X-ray-background (NXB) maps. For each ObsID, the FWC event files were reprojected using task `evproject` to match the observation. NXB maps were scaled to match the NXB level of each count image. For MOS, the scale factor was calculated using the ratio of out-of-field-of-view (OoFoV) count rates. For pn, even the OoFoV area can be contaminated by soft protons, and it cannot be used for an accurate rescaling of the NXB (Gastaldello et al. 2017; Zhang et al. 2020; Marelli et al. 2021). On the other hand, the pn instrumental background shows a similar long-term variability to that of Chandra's ACIS-S3 chip; therefore, we used this information for rescaling the pn NXB level in the observations (details are provided in Zhang et al., in preparation).

The corresponding exposure maps were generated using the task `eexpmap` with parameter `withvignetting=yes`. Point sources were detected and filled by the tasks `wavdetect` and `dmfilth` in the Chandra Interactive Analysis of Observations (CIAO) v4.13 package. We stacked individual count maps, exposure maps, and NXB maps, respectively, using the 0.5–2.0 keV energy band. We divided the NXB-subtracted count image by the exposure map to generate the flux map. After removing the instrumental background and correcting for telescope vignetting, a constant sky background was further subtracted from the images. The level of this background was estimated from the median flux in an annulus spanning radii of 60′–70′. Note that Mirakhor & Walker (2020) do detect a signal from the Coma ICM even at these large radii, albeit in a narrower energy interval of 0.7–1.2 keV, where the signal-to-background ratio is optimized. The sky background used here may therefore be slightly overestimated, but this does not have an impact on the radii of interest considered in our XMM-Newton analysis (limited in this case mostly within the cluster's R_{500}).

We furthermore used the four archival observations of the Coma cluster performed in 1991 June by the ROSAT Position Sensitive Proportional Counter (PSPC). These pointings extend out to radii of 60′–70′, totaling a clean exposure time of 78 ks. The data reduction was performed exactly as already described in Simionescu et al. (2013) and Bonafede et al. (2021). The low instrumental background of ROSAT makes these data an important complement to XMM-Newton in the faint cluster outskirts.

2.3. Planck Data

We used six Planck frequency maps acquired by the High Frequency Instrument (HFI) and the corresponding energy responses released in 2018 by the Planck collaboration (Planck Collaboration et al. 2020). The average frequencies of the HFI maps are 100, 143, 217, 353, 545, and 857 GHz. The nominal angular resolutions of the maps are $9\farcm69$, $7\farcm30$, $5\farcm02$, $4\farcm94$, $4\farcm83$, and $4\farcm64$, respectively. Following prescriptions of Galactic thermal dust studies performed by the Planck Collaboration (Planck Collaboration et al. 2014), we corrected HFI maps for individual offsets that maximize their spatial correlation with neutral hydrogen density column measurements performed in regions of the sky characterized by their low dust emissivity and by the exclusion of prominent SZ sources.

This multi-frequency data set allowed us to map the thermal SZ Compton parameter in a 4 deg^2 sky area centered on Coma, following the spectral imaging algorithm described in Baldi et al. (2019). Briefly, the Compton parameter, y, is jointly mapped in the wavelet space with the Cosmic Microwave Background anisotropies and with the Galactic thermal dust emissivity. This is achieved via a spatially weighted likelihood approach that includes the smoothing effect of individual HFI beams in the reconstruction of B3-spline wavelet coefficients. In order to best restore anisotropic details, a curvelet transform is eventually computed from these wavelet coefficients and denoised via a soft thresholding that we parameterize as a function of local values of the noise standard deviation. The resulting y-map has a resolution (FWHM of the point-spread function) of 5′, i.e., a factor 2 higher than the one published in Planck Collaboration et al. (2013).

2.4. WSRT Data

We use data from the Westerbork Synthesis Radio Telescope (WSRT) at ∼325 MHz. Part of these data come from the

---

[17] http://xmm-tools.cosmos.esa.int/external/xmm_user_support/documentation/sas_usg/USG/removingOoTimg.html

Table 3
Source Properties at 144 MHz

Source Name	Dist.	LAS	$S_{144\ \mathrm{MHz}}$	$P_{144\ \mathrm{MHz}}$
			Jy	W/Hz
Halo	⋯	71′–2.00 Mpc	12 ± 2	$1.5 \pm 0.2 \times 10^{25}$
Accretion relic	2°1–3.55 Mpc	55′–1.5 Mpc	0.47 ± 0.07	$5.7 \pm 0.9 \times 10^{23}$
Relic	73′–2.0 Mpc	38′–1.1 Mpc	2.4 ± 0.4	$3.0 \pm 0.4 \times 10^{24}$
NAT–relic connection	79′–2.3 Mpc	10′–280 kpc	0.7 ± 0.1	$9 \pm 1 \times 10^{23}$

Note. Column (1): name of the diffuse source. Column (2): distance from the cluster center. Column (3): largest angular size measured above the $2\sigma_{\mathrm{rms}}$ contour. Column (4): flux density measured above the $2\sigma_{\mathrm{rms}}$ contour. Column (5): radio power at 144 MHz. The K-correction is applied assuming $\alpha = -1, -1, -1.2$, and -1.4 for the halo, accretion relic, relic, and NAT–relic connection, respectively.

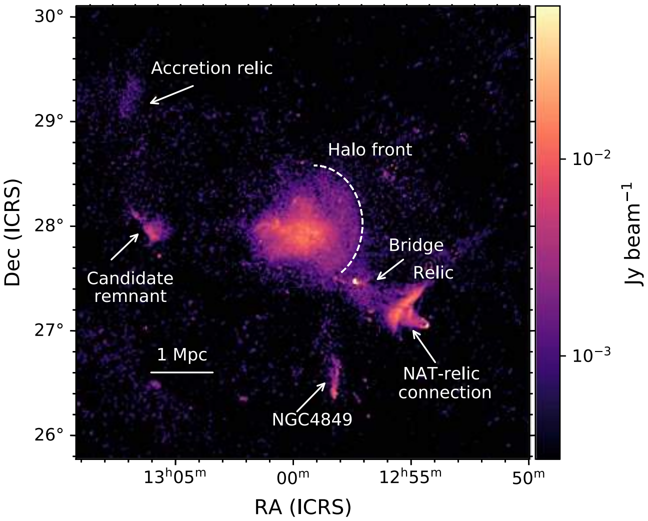

Figure 2. LOFAR emission of the Coma field at the resolution of 1′. The candidate accretion relic, halo front, bridge, relic, and NAT–relic connection are labeled.

observations published in Venturi et al. (1990) and Giovannini et al. (1991), which we have reimaged as explained in Bonafede et al. (2021). In this work, we also use more recent WSRT observations published by Brown & Rudnick (2011) that recover a larger fraction of the radio halo but are more affected by imaging and calibration artifacts due to the presence of the source Coma A, north of the relic. Brown & Rudnick (2011) observations are used here to study the spectral properties of the halo, while Venturi et al. (1990) and Giovannini et al. (1991) observations are used here to study the spectral index in the relic region. In Table 2, these images and their main properties are listed. We refer to the image published by Brown & Rudnick (2011) as WSRT H, as it is used to study the halo emission, and to the image published by Venturi et al. (1990) and Giovannini et al. (1991) as WSRT R, as it is used to study the relic region.

3. Components of the Diffuse Emission

The radio emission from the Coma field consists of several different components, either associated with the ICM or originating from the interaction of the radio galaxies with the environment. In Figure 2, the diffuse emission from the Coma cluster field is shown, after the subtraction of radio galaxies and point sources. The most relevant features are labeled. As already known, the Coma cluster hosts a radio halo, a radio relic, and a bridge of low surface brightness emission connecting the two. In addition to these components, several new features are detected in our LOFAR observations. In this section, we present the emission from the diffuse sources as imaged by LOFAR at 144 MHz. An analysis of their properties that includes radio images at other frequencies and the comparison with the X-ray emission from the ICM is presented in the following sections for each source separately.

3.1. The Radio Halo

At 144 MHz, the radio halo appears larger than at higher frequencies, with a Largest Angular Scale (LAS) of 1°2, measured east to west, corresponding to ∼2 Mpc (see Table 3). The halo appears to be composed of a central, bright core and a larger, weaker component that is asymmetrical and more pronounced toward the west (see Figure 3). The inner portion of the halo is what we define the "halo core."[18] This part of the halo is the one visible in the LoTSS images that impose an inner *uv*-cut of 80λ, corresponding to ∼43′. The 20″ resolution of LoTSS, here reproduced using the same *uv*-range restriction, provides a detailed image of the inner portion of the halo. Clearly, the emission from the halo core is brighter than the rest, and its surface brightness is characterized by bright filaments of radio emission, marked with arrows in Figure 3. Despite being the best studied radio halo, this is the first time that features such as these filaments are detected in its diffuse emission.

Outside the halo core, low surface brightness emission is detected, which is brighter toward the west. We call this emission the "outer halo" and discuss in Sections 4 and 6 whether the halo core and the outer halo show different properties, as recently proposed for some cool-core clusters (Savini et al. 2018, 2019; Biava et al. 2021; Riseley et al. 2022). The emission from the outer halo is only visible when baselines shorter than 80λ are included in the image, and hence it is filtered out in the LoTSS images.

In the right panel of Figure 3, we show the halo in the LOFAR 35″ image, after the subtraction of the unrelated radio sources. To the west, the halo has a sharp edge coincident with the halo front (see Figure 2 for labeling) already found by Brown & Rudnick (2011) and coincident with the shock front detected in the X-rays (Simionescu et al. 2013) and SZ (Planck Collaboration et al. 2013). In Figure 4 we show the radio profile computed in annuli across the halo front in comparison with the rest of the cluster. The two sectors have azimuth angles from 47° to 287° (Coma) and from 323° to 48° (front, centered in R.A. = 12:59:07, decl. = +28:01:31). The southwest (SW) part of the halo, toward the radio bridge, has been

---

[18] The halo core and outer halo are labeled in Figure 11.

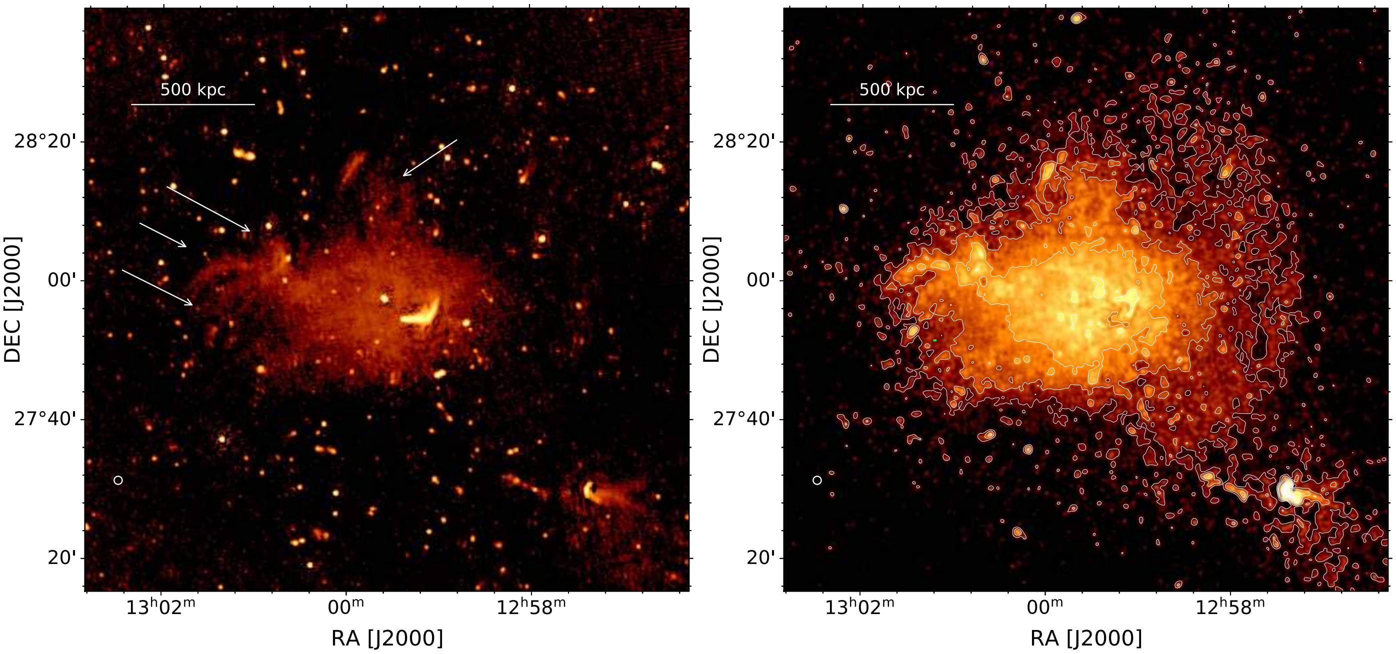

Figure 3. Left panel: zoom-in of the radio halo from the 20″ image, which is made imposing an inner *uv*-cut (image LOFAR as LoTSS 20 in Table 2). The halo core and the radio galaxies both of Coma and of the field are visible. The black bowl around the core indicates that large-scale diffuse emission is filtered out. White arrows mark the filaments (three arrows on the left) and the radio loop (arrow on the upper right). Right panel: same as the left panel, but from the 35″ image, where all the baselines have been included in the image and the discrete sources have been subtracted (see text for details) The outer halo and the halo front are well visible. Contours start at $3\sigma_{\rm rms}$ and are spaced by a factor of 2.

excluded. While the average cluster profile shows a smooth radial decline, a sharp edge is visible around ∼1900″ from the cluster center, coincident with the radio front found by Brown & Rudnick (2011).

Toward the SW, the spherical front continues and its brightness becomes weaker and merges with the emission from the radio bridge. The total flux density of the radio halo, measured from the images above $2\sigma_{\rm rms}$, is 10 ± 2 Jy at 144 MHz. The main properties of the radio halo are listed in Table 3.

3.2. The Radio Relic and The NAT–Relic Connection

To the SW of the Coma cluster, a radio relic has been discovered by Ballarati et al. (1981) and studied by several authors afterward (Venturi et al. 1990; Giovannini et al. 1993; Brown & Rudnick 2011; Bonafede et al. 2013; Ogrean & Brüggen 2013). However, the presence of the bright source Coma A, at the northwest (NW) of the relic, has always made its study difficult. Residual calibration errors remain in the LOFAR image (see Figure 5) and make it difficult to determine whether the relic extension to the NW is real. We note that the same extension has also been detected by single-dish observations at 1.4 GHz, where it also appears polarized (Brown & Rudnick 2011). Despite this, because of its questionable nature, we adopt a conservative approach and do not include it in our discussion of the relic.

The radio relic has an LAS of 38′, corresponding to ∼1.1 Mpc at the Coma redshift. Its emission is connected on both sides to two head–tail radio galaxies, namely, NGC 4839 to the northeast (NE) and NGC 4789 to the SW of the relic. From NGC 4839, we detect diffuse emission that blends into the bridge and relic emission (Bonafede et al. 2021). The surface brightness of the relic is not uniform but composed of patchy and filamentary substructures (see Figure 5). Stripes of radio emission depart from the relic and are directed toward the bridge and NGC 4839. A similar stripe is detected also near the tail of NGC 4839, directed toward the relic. These features could be regions where the magnetic field has been amplified and/or where the plasma has been stripped from the tail of NGC 4789. The surface brightness of these stripes is a factor 2–3 higher than the nearby emission, and their size is ∼11′.7, which corresponds to 300 kpc at the Coma's redshift.

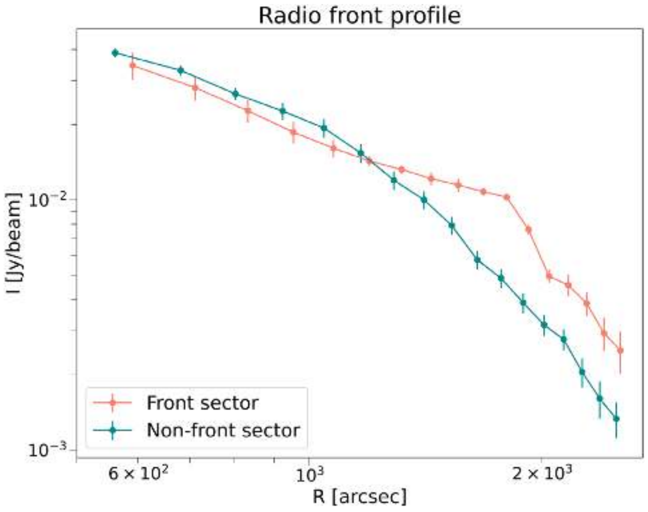

Figure 4. Radio profile of the Coma halo from the LOFAR image at 2′ resolution across the halo front in comparison with the rest of the halo. Error bars represent statistical errors only.

Beyond the relic, toward the SW, the narrow angle tail (NAT) galaxy NGC 4789 appears connected to the relic, as already found by, e.g., Giovannini et al. (1991). The connection between the relic and NGC 4789 has been interpreted as the tail of NGC 4789 feeding the relic with radio plasma

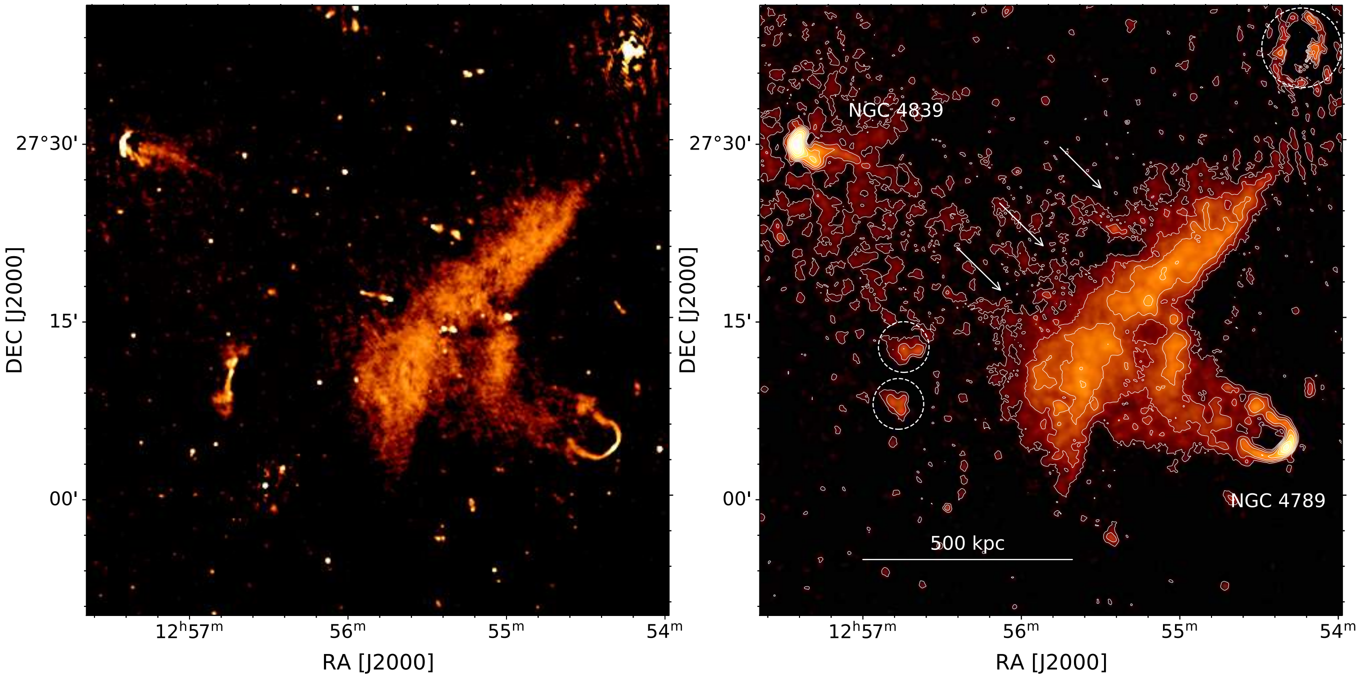

Figure 5. Zoom-in of the radio relic region. Left panel: 6″ image showing the complex emission that links the source NGC 4789 to the relic emission. Right panel: 35″ image. The source NGC 4789 is labeled. Arrows mark the position of the stripes that depart from the relic toward NGC 4839. White dashed circles indicate residuals from the subtraction of the lobes of NGC 4827, a Coma radio galaxy, and Coma A. Contours start at $3\sigma_{\mathrm{rms}}$ and are spaced by a factor of 2.

(e.g., Enßlin & Gopal-Krishna 2001). In Section 10, we will investigate the possible origin of this emission.

3.3. Diffuse Emission from NGC 4849

To the south of Coma, we detect diffuse emission, elongated in the north–south direction, with a size of $\sim 27'$. This emission seems associated with the radio galaxy NGC 4839, located at $\mathrm{R.A.} = 12^{\mathrm{h}}58^{\mathrm{m}}12\overset{\mathrm{s}}{.}679$, $\mathrm{decl.} = +26^{\mathrm{d}}23^{\mathrm{m}}48\overset{\mathrm{s}}{.}77$, at redshift $z = 0.01966$. Its angular size translates into a linear size of $\sim$650 kpc (see Figure 6). From the 6″ resolution image, the core of NGC 4849 is visible, and a hint of jet emission in the north–south direction is also present. A second bright component is located at the south of the core, which could be either an unrelated radio source seen in projection or the lobes of NGC 4849. The maximum extension of this tail in the WSRT image is $\sim 7'$. Using the WSRT H and “LOFAR as WSRT H” images (see Section 2 and Table 2) and taking into account the higher noise of the WSRT image in that region, we derive a 2σ limit for the spectral index of the tail $\alpha < -2$. Analyzing the emission of this source is not the aim of this paper; we note that similar steep spectrum tails have been found in the outskirts of other clusters (e.g., A1132, Wilber et al. 2018; A2255, Botteon et al. 2020a), likely tracing the motion of the galaxy in the ICM. The long tail of aged cosmic-ray electrons (CRe) left behind by these sources during their motion provides seed electrons that could be re-accelerated by turbulence and shocks.

3.4. Accretion Relic

After the subtraction of unrelated sources, two extended patches of diffuse emission are visible at the periphery of Coma, to its NE and east (see Figure 7). The diffuse component at the eastern side of Coma is not associated with any Coma cluster galaxy (Pizzo 2010). Pizzo (2010) also noticed that this source lies at the crossroads of two filaments of galaxies, pointing toward the clusters A2197 and A2199, respectively, and suggested that this emission could be due to the accretion of matter toward the Coma cluster. Our images have a higher resolution and allow us to recognize a double-lobe structure that resembles a radio galaxy. However, no core is obviously associated with it in the 6″ and 20″ images (see Figure 7). We tentatively label this source as a “candidate remnant”, but we note that its classification remains uncertain. Indeed, given its large angular size ($\sim 27'$) and the lack of an optical identification at the Coma cluster redshift, it would have a very large linear size if it were in the background of Coma.

The other diffuse patch in the NE part of Coma is entirely new and has an arc-like morphology and a weak uniform brightness. This emission does not appear connected to any discrete source (see Figure 7). When convolving the image to a resolution of 2′, it has a largest angular size of $\sim$55’, which would correspond to 1.5 Mpc at the cluster redshift, and it is located at $\sim 2\overset{\circ}{.}1$ from the cluster center. At the Coma redshift, this distance corresponds to $\sim$3.6 Mpc, while the cluster virial radius[19] is $\sim$2.9 Mpc. Since recent studies (e.g., Malavasi et al. 2020) have found an intergalactic filament of galaxies in the NW direction from the Coma cluster, this source could be connected to the cluster and its large-scale environment. Hence, we consider it plausible that this is an “accretion relic,” though more data supporting our hypothesis are needed. Considering that accretion shocks on these scales should be characterized by a strong Mach number ($\mathcal{M} \gg 5$; e.g., Hong et al. 2014), a strong prediction in this case would be that the radio spectrum of this emission should be $\alpha \propto \nu^{-1}$ and also characterized by a large degree of polarization. The properties of this accretion relic are listed in Table 3.

---

[19] R_{100} is considered here to be a good approximation of the virial radius, as the cluster redshift is 0.023.

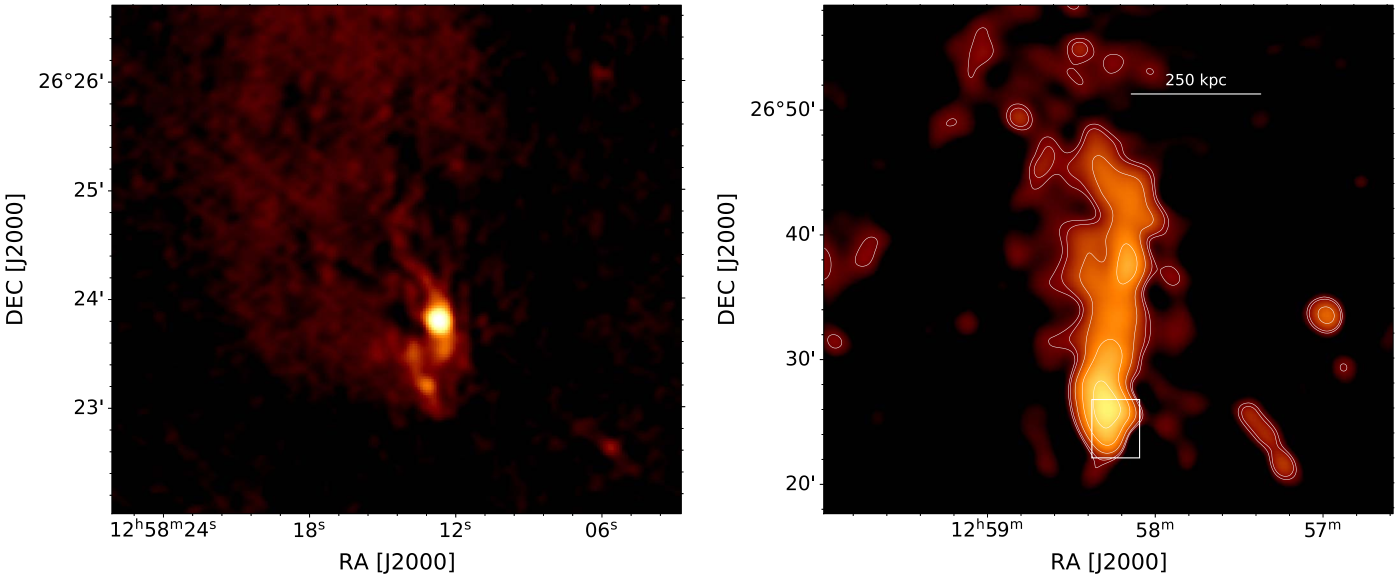

Figure 6. Zoom-in of the region of NGC 4849, to the south of Coma. Left panel: 6″ image from LoTSS showing the core of NGC 4849. Right panel: 1′ image showing the full extent of the tail. The white box marks the region shown in the left panel. Contours start at 3σ and are spaced by a factor 2.

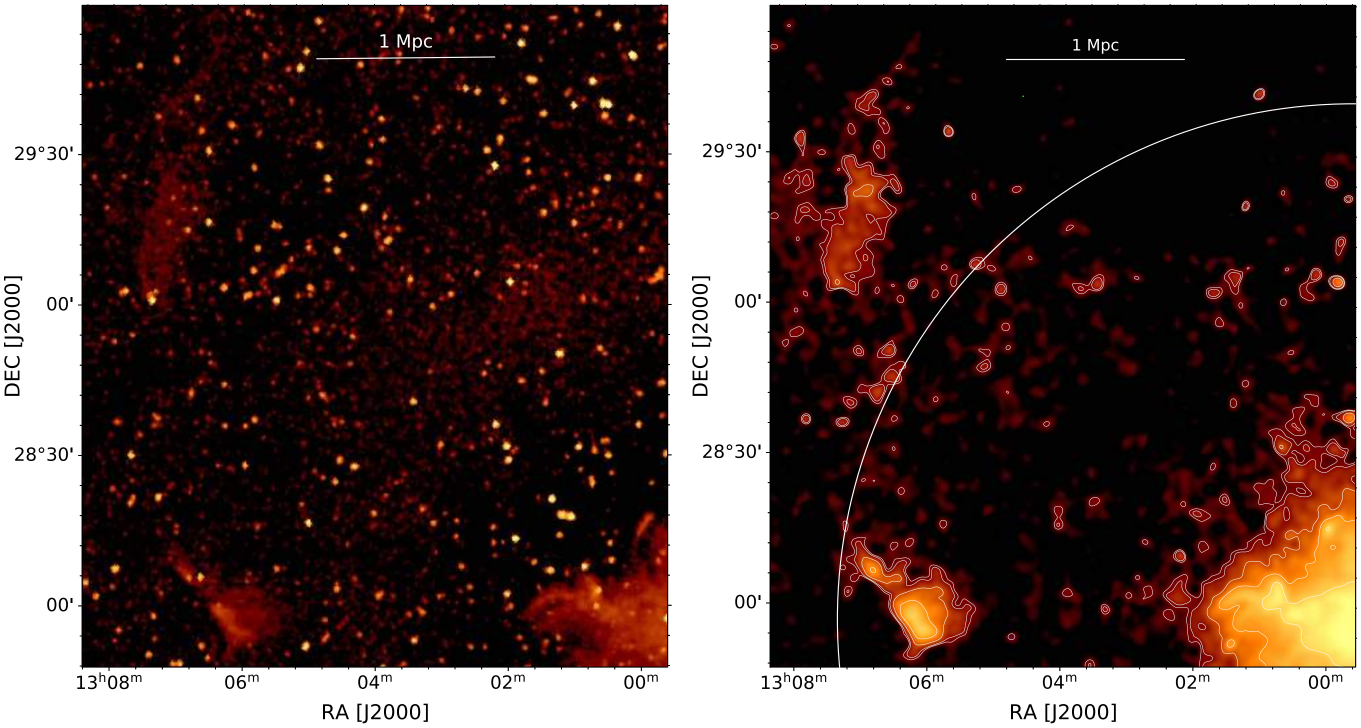

Figure 7. Zoom-in of the region of the accretion relic. Left panel: 20″ image from LoTSS showing the diffuse emission of the accretion relic (upper left), the candidate remnant source (lower left), and all the radio sources in the field. Right panel: same as the left panel, but from the 2′ image. Contours are plotted at (3, 4, 8, 16, 32, 64) $\sigma_{\rm rms}$. The white circle is centered on the Coma cluster centre and has a radius $r = R_{100}$.

4. The Radio Halo Profile

To characterize the halo properties, we have fitted its surface brightness profile adopting the approach first proposed by Murgia et al. (2009) and more recently generalized by Boxelaar et al. (2021) to account for asymmetric halo shapes. The main novelty of this procedure is that the profiles are fitted to a two-dimensional image directly, using MCMC to explore the parameter space, rather than to a radially averaged profile. In addition, the fitting procedure by Boxelaar et al. (2021) allows one to fit also elliptical and skewed (asymmetric) models. We refer to Boxelaar et al. (2021) for a detailed explanation and summarize here the relevant parameters. The surface brightness model is given by

$$I(r) = I_0 \exp^{-G(r)}, \tag{1}$$

where I_0 is the central surface brightness and $G(r)$ a radial function. $G(r) = \left(\frac{|r^2|}{r_e^2}\right)^{0.5}$ for the circular model, while $G(r) = \left(\frac{x^2}{r_1^2} + \frac{y^2}{r_2^2}\right)^{0.5}$ for the elliptical models, where r_e is the

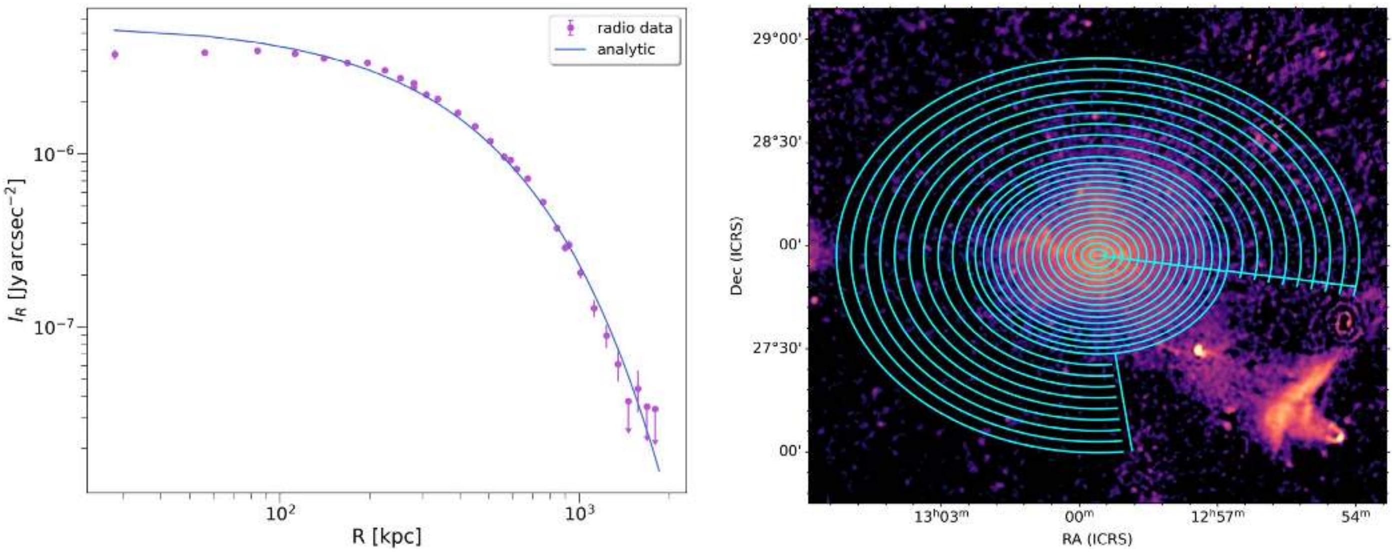

Figure 8. Left panel: circles are the radio average brightness profile of the radio halo, computed within elliptical annuli having major- and minor-axis sub-multiples and multiples of r_1 and r_2, i.e., the minor and major axis of the elliptical exponential fit (see Table 4). The SW sector of the halo has been blanked for ellipses with major and minor axis larger than $3r_1$ and $3r_2$, respectively, to exclude the bridge region. Error bars represent the error on the mean; upper limits at 3σ are plotted as arrows. The width of the annuli goes from 1′ in the center to 4′ in the outer annuli, to improve the sensitivity to low surface brightness emission in the outer parts of the halo. The blue line refers to the best-fit elliptical model; see Table 4. Right panel: radio image of the Coma cluster at 1′ resolution. The inner cyan ellipse has major and minor axis equal to $3r_1$ and $3r_2$, respectively, and elliptical annuli are spaced by 1′. The outer elliptical bins have a width of 4′ and and trace ellipses out to $6r_1$ and $6r_2$, showing the SW region that has been excluded from the analysis because of the bridge.

Table 4
Radio Halo 2D Fit

LOFAR—144 MHz									
Halo model	χ^2_r	I_0 (μJy arcsec^{-2})	r_1 (kpc)	r_2 (kpc)	r_3 (kpc)	r_4 (kpc)	Angle (deg)	$S_{144,\mathrm{MHz}}$ (Jy)	$P_{144,\mathrm{MHz}}$ (10^{25} W Hz^{-1})
Circular	1.7	5.42 ± 0.04	310 ± 1					12.20 ± 0.04	1.470 ± 0.002
Elliptical	1.6	5.50 ± 0.02	355 ± 1	268 ± 1				12.21 ± 0.04	1.470 ± 0.005
Skewed	1.6	5.46 ± 0.01	337 ± 2	368 ± 2	207 ± 2	342 ± 2	2.99 ± 0.001	12.35 ± 0.05	1.490 ± 0.05
WSRT—342 MHz									
Halo model	χ^2_r	I_0	r_1	r_2	r_3	r_4	Angle	$S_{342,\mathrm{MHz}}$	$P_{342,\mathrm{MHz}}$
Circular	0.7	3.52 ± 0.08	255 ± 4					5.3 ± 0.1	0.64 ± 0.01
Elliptical	0.7	3.54 ± 0.08	268 ± 5	240 ± 6				5.3 ± 0.1	0.64 ± 0.01

Note. Column (1): model used. Column (2): reduced χ^2 value. Column (3): central brightness of the fit. Columns (4)–(7): e-folding radii. Column (8): angle for the skewed halo model fit. Column (9): total halo power at 144 MHz computed within $3r_e$. Only statistical fit errors are shown in the table.

characteristic e-folding radius, and $r^2 = x^2 + y^2$. The skewed model allows for an off-center maximum of the brightness distribution and is characterized by four different scale radii (r_1, r_2, r_3, r_4) and by an angle to describe the asymmetric brightness distribution.

We have investigated these three profiles (circular, elliptical, and skewed), and results of the fit are given in Table 4. In this table, we only list the statistical error, while the systematic one is 15% of the listed flux density and due to the uncertainty on the absolute flux scale. All models give a consistent total radio power ($P_{144\mathrm{MHz}} \sim 1.47 \times 10^{25}$ W Hz^{-1} computed within 3 times the e-folding radius) and central radio brightness ($I_0 \sim 5\ \mu$Jy arcsec^{-2}). We note that the flux density and consequently the power measured by the fit are in perfect agreement with the estimate derived from the images above $2\sigma_{\mathrm{rms}}$ (see Section 3). As the reduced χ^2 values are similar in the skewed and elliptical model, we consider the latter in the following analysis.

In Figure 8, we show the radial profile of the halo brightness at 144 MHz. We have computed the mean of the radio brightness and its error within elliptical annuli having a width that changes progressively from 1′ in the center to 4′ in the outer regions, to maximize the resolution at the center and the sensitivity to low surface brightness emission in the halo peripheral regions. The bridge region is excluded starting from elliptical annuli with major and minor axis larger than $3r_1$ and $3r_2$, respectively. We considered upper limits the values where we have a mean smaller than 3 times the rms noise. From this plot, we derive that we have detected the halo emission up to $r \sim 1.3$ Mpc, which corresponds to $\sim 4.5r_1$ and r_2 (see Table 4).

In the following, we refer to the halo core as the emission contained within an ellipse having as major and minor axis r_1 and r_2, respectively, and to the outer halo as the emission contained within $4r_1$ and $4r_2$, excluding the halo core. We note that the halo core and outer halo are well represented by a single exponential model and do not need to be considered as

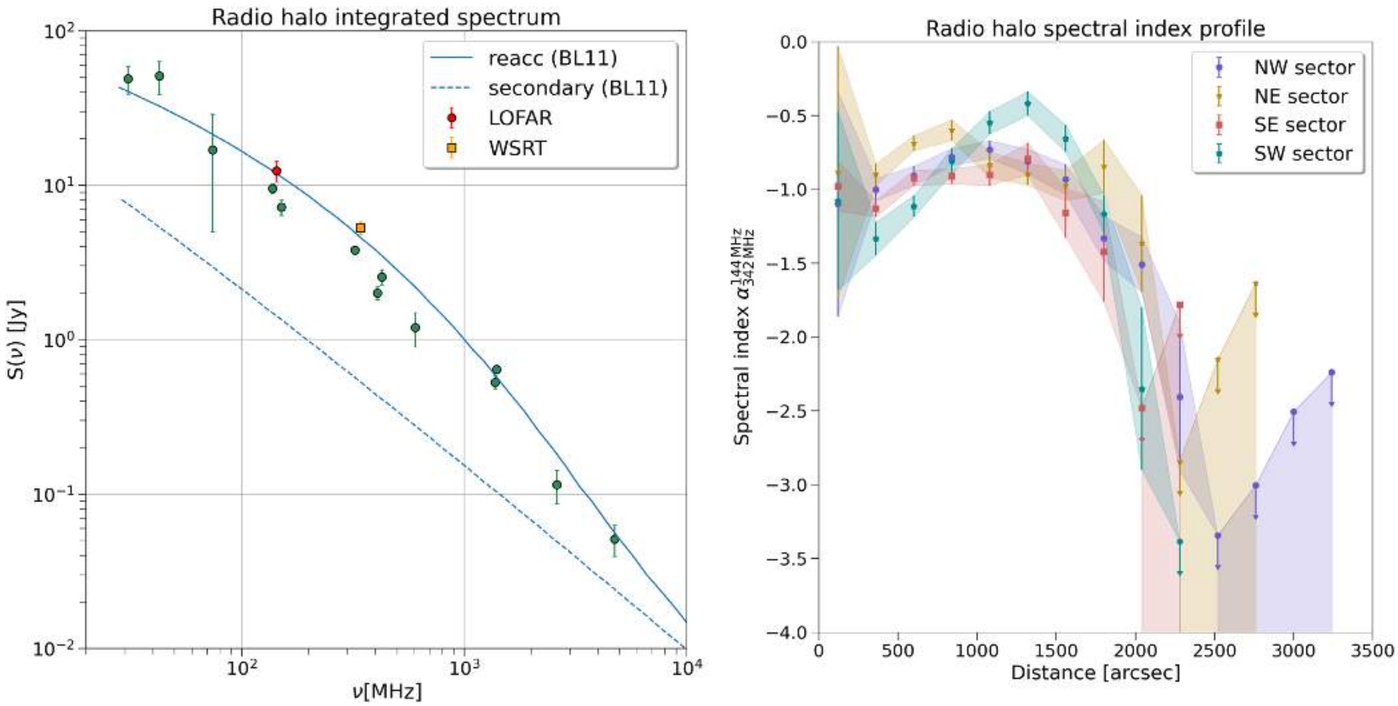

Figure 9. Left: integrated spectrum of the radio halo from literature data (green circles) from Thierbach et al. (2003 and references therein), as corrected and rescaled by Brunetti et al. (2013). The new LOFAR measurement (red circle) and the WSRT measurement (orange square) are shown, measured within 3 times the effective radii as derived by the halo fit (see text for details). The solid line shows expectations from a model where secondary particles are re-accelerated by compressive turbulence (Brunetti & Lazarian 2011). The dashed line shows the spectrum computed from secondary emission, after 200 Myr since turbulent re-acceleration has been switched off (Brunetti & Lazarian 2011). Right: spectral index radial profile computed in the different sectors, as listed in the legend. Arrows are 3σ upper limits, only statistical errors are shown, and the values of the spectral index are also affected by the flux calibration uncertainties of WSRT and LOFAR (10% and 15%, respectively) that would contribute with an additional error of 0.2.

two separate components, if we consider the average surface brightness of the halo emission. However, as we show in the following analysis, they are characterized by different properties.

We applied the same fitting procedure to the WSRT image (WSRT H in Table 2), after blanking the sources that were contaminating the emission. We only attempted an elliptical and circular model fit. Results are listed in the bottom part of Table 4. Both fits give the same total flux density and radio power and have the same χ^2_r value, smaller than 1, possibly indicating that the errors are being overestimated. We note that the r_1 and r_2 values are slightly smaller than those found in the LOFAR image, indicating a more peaked profile of the radio emission and hence of the emitting CRe at higher frequencies.

5. Spectral Properties of the Radio Halo

5.1. The Integrated Spectrum

Using literature results and the halo flux density at 144 and 342 MHz, we can constrain the low-frequency part of the radio halo spectrum. The spectrum of radio halos provides important information about the underlying re-acceleration mechanism. Indeed, it allowed us in the past to conclude that a very steep spectrum ($\alpha < -1.5$, also called ultra–steep-spectrum halos) cannot be produced by hadronic models (e.g., Brunetti et al. 2008). Using the flux densities that result from the fits, we can measure the spectral index between 144 and 342 MHz, yielding $\alpha = -1.0 \pm 0.2$. Though residuals from sources could still be present, the fitting procedure we have used should minimize that contribution (Boxelaar et al. 2021); hence, a considerable impact to the whole halo emission is unlikely. We find that the spectrum is slightly flatter than previously reported in the literature, although still consistent within the errors. The spectrum of the halo in the Coma cluster has been extensively studied in the literature (e.g., Giovannini et al. 1993; Thierbach et al. 2003), using both interferometric images and single-dish data. At low frequencies, the contribution of radio galaxies is difficult to account for, for mainly two reasons: (i) the low resolution of observations published so far, and (ii) the larger extent of tailed radio galaxies whose emission blends with the halo emission. Our sensitive and high-resolution LOFAR images allow us to alleviate both of these problems. In addition, we now have a more accurate method to estimate the halo flux density. We have collected the data available in the literature, i.e., those presented in Thierbach et al. (2003) and rescaled to the same absolute flux scale as in Brunetti et al. (2013), and added our measurement at 144 MHz. In Figure 9 we show the spectrum of the halo. Green circles refer to values taken from Brunetti et al. (2013) and do not refer to the same aperture radius. The red and orange circles refer to the LOFAR and WSRT maps, respectively, computed within the same aperture (corresponding to three *e*-folding radii of the LOFAR image; see Table 4). In Figure 9, left panel, we show one possible spectrum that would be produced by re-acceleration models. However, for a proper derivation of the halo spectral properties, one should compare the flux densities from images done with the same *uv*-range, the same procedure for compact source subtraction, and using the same aperture radius. We also note that using a fitting algorithm, such as the one proposed by

Boxelaar et al. (2021) and used here, would also minimize the effect of different noise obtained at different frequencies.

Recently, Rajpurohit et al. (2022) have shown that the hint for a spectral break claimed in the radio relic of A2256 below 1.4 GHz (Trasatti et al. 2015) is not confirmed once the analysis is performed with matching *uv*-coverage and unrelated sources are subtracted properly. In the case of the Coma halo, we note that the high-frequency measurements are almost a factor 10 below the value extrapolated from a power law at low frequencies. However, the exact shape of the spectrum could be affected by the effects mentioned above. In addition, it is important to get a precise flux density at frequencies below 100 MHz to characterize the integrated radio spectrum. Here data from the LOFAR Low-Band Antennas (LBA) will provide powerful constraints.

5.2. Spectral Index Profile

Using WSRT and LOFAR HBA data, we can obtain a radial profile of the halo spectral index. A steepening of the radial profile has been found by Giovannini et al. (1993) using data between 326 MHz and 1.38 GHz. They found that the radio halo has a smooth spectrum in the central regions (inner 480″ radius) with $\alpha \sim -0.8$ and a steeper value ($\alpha \sim -1.2$ down to -1.8 in the outer regions).

Using WSRT and LOFAR HBA images, we can now compute the spectral index profile out to larger distances. We have reimaged the LOFAR data using only baselines larger than 40 m, i.e., the shortest WSRT baseline, and convolved the LOFAR image to the same resolution as the WSRT image. The sources embedded in the diffuse emission are subtracted from the WSRT image; however, as some residuals were still present, we applied the multi-filtering technique described in Rudnick (2002) and blanked the WSRT image wherever the filtered image was above 3 mJy beam^{-1}. We blanked the LOFAR image accordingly. We have divided the radio halo into four sectors (NW, NE, SE, and SW) and computed the mean spectral index α in elliptical annuli having the major and minor axis proportional to r_1 and r_2, up to the maximum distance where the halo is detected (see Section 4 and Figure 8).

The four outermost annuli of the SW sector have been removed to exclude the bridge region. We have computed the spectral index in each annulus and considered upper limits the annuli that have a total flux density smaller than $3\sigma_{\rm rms} \times \sqrt{(N_{\rm beams})}$, with $N_{\rm beams}$ being the number of independent beams sampled in each annulus. As the radio halo is more extended in the LOFAR image than in the WSRT image, we mainly derive upper limits at distances larger than ~2000″ (950 kpc). The radial trend of the spectral index is shown in the right panel of Figure 9. We note that values in some annuli are surprisingly flat, possibly because of residual contamination from unrelated sources. The increasing values of the upper limit in the outer annuli are due to the larger area sampled by the annuli. All the sectors show a spectral index that becomes steeper at distances of ~1500″ from the cluster center. In the SW sector, we also clearly detect a steepening toward the cluster center. A similar, though less pronounced, trend is also observed in the other sectors, though we note that in the NE sector the radial profile of α is more complex, and no clear trend at distances smaller than $r \sim 2000''$ can be established. The SW sector is affected by the passage of the NGC 4839 group; hence, is it possible that different physical conditions are present there. Overall, we can conclude that the spectral trend is characterized by clear steepening at the cluster outskirts and a mild steepening toward the cluster center.

In the next section we will discuss the physical implications of these results in the framework of turbulent re-acceleration models.

5.3. Radial Variations of The Spectral Index and Re-acceleration Models

In the presence of a break in the integrated spectrum of radio halos, homogeneous re-acceleration models predict that increasingly steeper spectra will be seen at increasing distance from the cluster center (Brunetti et al. 2001). Assuming homogeneous conditions, the frequency at which steepening occurs, ν_s, is proportional to

$$\nu_s \propto \tau_{\rm acc}^{-2} \frac{B}{(B^2 + B_{\rm IC}^2)^2}, \tag{2}$$

where $\tau_{\rm acc}$ is the re-acceleration time (see Cassano & Brunetti 2005; Brunetti & Lazarian 2007), which depends on the assumed turbulent properties and re-acceleration mechanism. $B_{\rm IC}$ is the inverse Compton equivalent magnetic field. In the case of a constant $\tau_{\rm acc}$, the steepening frequency depends only on the magnetic field strength. To better follow the discussion below, let us define a critical magnetic field value

$$B_{\rm cr} = \frac{B_{\rm IC}}{\sqrt{3}} \sim 2\ \mu{\rm G}.$$

As long as $B < B_{\rm cr}$, one expects to see a radial steepening of the spectral index at distances larger and larger from the cluster center as we move toward lower observing frequencies. This is what we observe beyond a radius of ~30′. Giovannini et al. (1993) also detected a steepening between the higher frequency pair 325 MHz and 1.38 GHz, beyond a radius of ~8′ from the cluster center. While we do expect more dramatic steepening at the higher frequencies, whether these two sets of measurements are consistent with a single physical model requires further investigation.

Moreover, we detect for the first time a steepening of the spectral index toward the cluster center. This can also be explained in the framework of homogeneous re-acceleration models, if in the cluster center we have $B > B_{\rm cr}$. Assuming a magnetic field profile as derived from rotation measure (RM) studies ($B \propto B_0 n_e^{0.5)}$; Bonafede et al. 2010), we have indeed a central magnetic field of $B_0 \sim 5\ \mu$G, and hence $B > B_{\rm cr}$. We note that a similar steepening toward the cluster center should be visible also in the higher frequency spectral index map by Giovannini et al. (1993). However, in that work the authors only report a spectral index trend through a line passing from the cluster from SE to NW. It is possible that a radial analysis similar to the one we present here would show the same trend. Alternatively, one should think of ad hoc re-acceleration conditions that make this steepening visible only at low frequency. Future observations at higher frequencies could shed light on this point.

We can conclude that the data presented in this work, together with literature data by Giovannini et al. (1993) and Bonafede et al. (2010) provide a coherent picture with the expectations from homogeneous turbulent re-acceleration models (Brunetti et al. 2001), though the spectral index trend in the cluster center leaves some open questions that could be addressed by future observations.

5.3.1. Toward a Constraint of The Re-acceleration Model Parameters

Constraining the model parameters, such as $\tau_{\rm acc}$, would require a detailed 3D modeling and a precise constraint on the radial position of ν_s. However, we can try to make first-order calculations to see whether the qualitative coherent picture outlined above is quantitatively supported. Giovannini et al. (1993) have detected a spectral steepening at $\sim 8'$ between 326 MHz and 1.38 GHz. Assuming a central magnetic field $B_0 = 4.7$ μG, one would expect to detect the steepening between 144 and 342 MHz, where the magnetic field is $B \sim 0.7$ μG, i.e., at $r \sim 2$ Mpc ($\sim 71'$) from the cluster center. Instead, the steepening is detected at $r \sim 30'$ from the cluster center, i.e., a factor 2 closer to the expected location. This may suggest that $\tau_{\rm acc}$ is not constant and increasing with the distance from the cluster center. Though this result is not surprising from a theoretical point of view, it would be the first time that data support this claim. Instead of a constant $\tau_{\rm acc}$, we can make a step further and assume a constant turbulent Mach number $\mathcal{M}_t$. In this case, the steepening frequency is proportional to

$$\nu_s \propto T^{2a} \frac{B}{(B^2 + B_{\rm ICM}^2)^2}, \tag{3}$$

where T is the cluster temperature and a is a constant that is $a = 1$ for re-acceleration via Transit-Time-Damping mechanism with compressive turbulence and $a = 1.5$ for non-resonant second-order acceleration with solenoidal turbulence[20] (Brunetti & Lazarian 2016). In order to explain the spectral index steepening at $r \sim 30'$ from the cluster center, the temperature should be $\sim$35–45% lower at a distance of $30''$ than at a distance of $8'$, where the steepening is detected at higher frequency. We note that this temperature drop is consistent with the temperature profile found by Simionescu et al. (2013).[21] We stress again that the calculations we have just performed do not allow us to make any claim, as long as ν_s is not precisely determined from data and projection effects are not taken into account. However, they show that the qualitative picture outlined above is not at odds with first-order quantitative estimates.

6. Thermal and Non-thermal Correlations in the Radio Halo

6.1. Point-to-point Analysis

Investigating the point-to-point correlation between the radio and the X-ray surface brightness can give important information about the relation between the thermal and non-thermal components of the ICM. In addition, it has the potential of constraining the mechanism responsible for the radio emission. Govoni et al. (2001) have first investigated this correlation for a small sample of radio halos, finding a sublinear scaling of the radio brightness with respect to the X-ray brightness. More recently, Botteon et al. (2020a), Rajpurohit et al. (2021a, 2021b), and Ignesti et al. (2020) have investigated the same correlation for radio halos and mini halos, respectively, finding that halos tend to have a sublinear or linear scaling and mini halos show linear or superlinear behaviors.

Table 5
Radio–X-ray Correlation for Different Gaussian Smoothing Lengths

Gaussian Beam	β	10%–90%	$\rho_{\rm P}$
FWHM			
1′	0.64	0.65–0.63	0.86
2′	0.65	0.66–0.63	0.88
3′	0.68	0.70–0.66	0.89
4′	0.70	0.73–0.68	0.88
5′	0.74	0.78–0.70	0.89
6′	0.76	0.81–0.72	0.88

Note. Column (1): FWHM of the smoothing Gaussian or restoring beam. Column (2): best-fit slope. Column (3): 10th and 90th percentile of the posterior distribution for β. Column (4): Pearson correlation coefficient.

Since the Coma radio halo is the one for which most spatially resolved and multiwavelength data are available, it is important to establish the statistical relation between its thermal and non-thermal components.

We have investigated the thermal to non-thermal correlation for the Coma cluster, fitting the radio (I_R) and X-ray (I_X) surface brightness in log–log space, according to

$$\log I_R = \beta \log I_X + \gamma, \tag{4}$$

where β is the correlation slope. We have used a hierarchical Bayesian model (Kelly 2007), which allows us to perform linear regression of I_R on I_X accounting for intrinsic scatter in the regression relationship, possibly correlated measurement errors, and selection effects (e.g., Malmquist bias). Using this method, we have derived a likelihood function for the data. We consider the mean of the posterior distribution as the best-fit slope. Following Botteon et al. (2020a) and Bonafede et al. (2021), we considered as upper limits the radio values that are below $2\sigma_{\rm rms}$.

Despite the fact that we detect the radio halo up to a distance of $\sim$1.3 Mpc, the analysis of the radio–X-ray correlation is limited by the extent of the XMM-Newton mosaic. In particular, because of soft-proton contamination, the analysis is restricted to a distance of $2400''$ ($\sim$1.1 Mpc) from the cluster center. To gain sensitivity toward the low surface brightness emission of the halo outskirts, we have convolved the radio image with Gaussian beams having FWHM of 1′, 2′, 3′, 4′, 5′, and 6′. We have computed the mean of the radio and X-ray brightness in square boxes having an area equal to a Gaussian beam of the radio image and computed the fit using X-ray images smoothed at the same resolution. We have considered upper limits the values that are below $2\sigma_{\rm rms}$, i.e., twice the noise of the radio image. The results of the fits are listed in Table 5 and the I_X-I_R correlation from the image at 6′ resolution is shown in Figure 10. The image at 6′ resolution allows us to recover the outermost regions of the halo keeping the highest possible resolution. I_X and I_R are positively correlated with a slope $\beta = 0.76^{+0.05}_{-0.04}$ and a Pearson correlation coefficient $\rho_{\rm P} = 0.89$. We note that the finest grid (boxes spaced by 1′) recovers a slope similar to the one initially found by

---

[20] In this case we consider also a constant Alfvén velocity, based on the scaling $B^2 \propto n$.

[21] We take as a reference the profile extracted along the east sector of their analysis, which is the only one not contaminated by the west shock and by the merger with the NGC 4839 group.